Bulletin of the Mineral Research and Exploration

http://bulletin.mta.gov.tr

Evaluation of the tectonic activity of faults with mineral alterations: a case of the East Anatolian Fault-Palu segment, Türkiye

Firdevs GÜZEL[a] and Gülcan SARP[a*]

[a] *Süleyman Demirel University, Faculty of Humanities and Social Sciences, Department of Geography, Isparta, Türkiye*

Research Article

Keywords:
Active Tectonics, Alteration Minerals, Getis-Ord Gi* Statistic, ASTER.

ABSTRACT

Palu segment is a part of the East Anatolian Fault Zone (EAFZ), the most important active left-lateral strike-slip fault system in Turkey, and there are different mineral alterations in this zone. The study tested the spatial relationship between tectonic activity and mineral alterations with the Getis-Ord Gi* statistic in and around the Palu segment. Mineral alterations at the pixel level were determined from ASTER images by Ratio, Relative Band Depth (RBD), Mineral Indices, CROSTA, Constrained Energy Minimization (CEM), Mixed Tuned Matched Filter (MTMF) methods. According to the results, the spatial distribution of alteration minerals extend parallel to tectonically active fault lines and/or partially bounded by faults in the area. RBD, Mineral Indices, CROSTA, CEM, and MTMF image processing algorithms applied in the study gave consistent results in the spatial determination and mapping of mineral alterations. At 99% and 95% confidence intervals, statistically significant cold spot clusters indicate the proximity of alterations to faults concentrated around fault lines. This degree of clustering of mineral alterations indicates regions with high alteration rates close to fault lines and areas with tectonic activity along fault lines.

Received Date: 09.05.2024
Accepted Date: 18.07.2024

1. Introduction

The East Anatolian Fault Zone (EAFZ) located in Eastern Turkey is a tectonically active fault system characterized by strike-slip movement. The Arabian and Anatolian plates are separated along a transform-type plate boundary (Arpat and Şaroğlu, 1972; Hempton, 1981). The fault system originates at the triple junction in Karlıova and progresses southwest until it reaches a second triple junction in the Amik basin, close to Antakya (Over et al., 2004, Figure 1a). There are different thoughts about the age of the fault system. According to some researchers, the age of the fault system is Late Miocene and Early Pliocene (Arpat, 1972; Şengör et al., 1985, Dewey et al., 1986; Hempton, 1987, Perinçek and Çemen, 1990; Lyberis et al., 1992), while others, it is Late Pliocene (Arpat and Şaroğlu, 1972; Şaroğlu et al., 1987, 1992*a, b*; Emre and Duman, 2007). Based on the geological data and GPS records the present slip rate of the EAFS varies 6-10 mm year^{-1} and 11 ± 2 mm year^{-1}, respectively (Reilinger et al., 1997; McClusky et al., 2000). On the other hand, Taymaz et al. (1991) estimated slip rates of 25-35 mm year^{-1} for the fault zone. Left-lateral strike-slip fault character of the EAFS is confirmed with geologic and geodetic studies (Arpat and Şaroğlu, 1972; Şaroğlu et al., 1992*a, b*; Reilinger et al., 1997; Herece, 2008; Duman et al., 2012; Duman and Emre, 2013) and seismological observations (McKenzie,

Citation Info: Güzel, F., Sarp, G. 2024. Evaluation of the tectonic activity of faults with mineral alterations: a case of the East Anatolian Fault-Palu segment, Türkiye. Bulletin of the Mineral Research and Exploration 175, 149-165. https://doi.org/10.19111/bulletinofmre.1518855

**Corresponding author: Gülcan SARP, gulcansarp@sdu.edu.tr*

1972; Taymaz et al., 1991; Örgülü et al., 2003; Gülerce et al., 2017; Güvercin et al., 2022).

Based on field studies and historical earthquakes, the East Anatolian Fault (EAF) system has been systematically divided into distinct segments by various researchers. Hempton (1981) identified five segments characterized by geological features, seismicity patterns, and structural characteristics observed along the fault zone. Barka and Kadinsky-Code (1988) expanded this segmentation to fourteen segments through detailed geological and geophysical studies. Şaroğlu et al. (1992*a, b*) proposed six segments based on their geological and tectonic analysis, while Herece (2008) delineated eleven segments using geological and geophysical data. Additionally, Duman and Emre (2013) defined seven segments based on their specific geological and geophysical findings. More recently, Bayrak et al. (2015) conducted comprehensive geological and geophysical studies resulting in a segmentation of five distinct segments. The Palu segment, which is one of the most striking fault segments mentioned in these studies, was chosen as the application area for this study (Figure 1b). According to Çetin et al. (2003), the Palu segment comprises small faults that run parallel to the main fault within a zone spanning 54 km in length and 5 km in width. In contrast, Duman and Emre (2013) describe this fault segment as being 77 km long and divided into three sub-sections. While previous studies have extensively covered the geology, activity, and characteristics of the faults in the area, there has been comparatively limited discussion regarding the mineral alterations within the region and their association with these faults. In recent years, increased access to multispectral satellite imagery has enabled the precise identification of mineral alterations at the pixel level and high spatial accuracy. This capability facilitates the association of these alterations with fault systems. Therefore, the approach proposed in this study is expected to offer a novel perspective on segmenting large fault systems like the EAFZ and correlating alteration minerals with the tectonic activity of faults.

In particular, the Advanced Space Source Thermal Emission and Reflection Radiometer (ASTER), a sensor launched by NASA in 1999 and located on the EOS/Terra platform has been an important resource for mapping mineral alterations. Because of the more diagnostic absorption properties of minerals in the visible and near infrared (VNIR), short wave infrared (SWIR), and thermal infrared (TIR) regions of the Electromagnetic Spectrum (EMS), ASTER data is frequently used in lithological mapping and mineral exploration. The VNIR component of the spectrum is crucial for the study of iron oxides and hydroxides because they often reflect more in the near-infrared (NIR) range than in the visible region (Hunt and Salisbury, 1974; Hunt, 1977; Yamaguchi and Naito, 2003). As a result of a larger number of bands in the SWIR area, ASTER is the first multispectral spaceborne sensor capable of differentiating OH-bearing minerals (Abrams and Hook, 1995). Based on their spectral signatures, several diagnostic groupings of hydrothermal minerals, mostly in the SWIR region of the electromagnetic spectrum, can be identified, including clays, phyllosilicates, sulfates, and carbonates (Hunt, 1977; Clark et al., 1990; Yamaguchi and Naito, 2003).

Depending on the improvements in remote sensing technologies from the past to present, different methods have been brought to the literature for pixel-based detection of mineral alterations from Multi-Spectral Scanner (MSS) images. Among these, the most widely used are Band Ratio, Relative Band Depth (RBD), Mineral Indices, CROSTA, Constrained Energy Minimization (CEM), Mixed Tuned Matched Filter (MTMF) methods (Holben and Justice, 1981; Crowley et al., 1989; Loughlin, 1991; Crowley, 1993; Harsanyi, 1993; Boardman et al., 1995; Farrand and Harsanyi, 1997; Sabins, 1999; Tangestani and Moore, 2002; Zhang et al., 2007; Kayadibi, 2008; Gabr et al., 2010; Wang and Zhang, 2011; Guha et al., 2014; Li et al., 2014; Pour et al., 2017, 2019; Tözün, 2021; Güzel, 2023).

In this study, the relationship between mineral alterations and active faults was evaluated through two distinct phases. Initially, alteration minerals were identified and extracted from ASTER images using a combination of methods including Band Ratio, RBD, Mineral Indices, CROSTA, CEM, and MTMF. Then,

the spatial relationship based on the distance between mineral alterations and fault lines was evaluated using the Getis-Ord Gi* statistic (Getis and Ord, 1992). This method helps in assessing the clustering and proximity of mineral alterations to fault lines, thereby elucidating the spatial relationship between geological processes and mineralogical changes.

The findings of this study revealed statistically significant cold spot values at both the 99% and 95% confidence intervals, highlighting a pronounced concentration of alteration minerals near fault lines. Moreover, the spatial distribution analysis of these identified alteration minerals indicated a parallel displacement relative to fault offset. These observations underscore the spatial relationship between mineral alterations and active faults, suggesting a direct influence of fault structures on the distribution and concentration of alteration minerals in the study area.

2. Geology of the Study Area

According to the 1/100.000 scaled geological maps produced by the Turkish Mineral Research and Exploration General Directorate (MTA), the oldest unit in the study area is the Paleozoic, and the youngest unit is Quaternary (Figure 1c). The oldest geological unit in the study area is the Bitlis metamorphics (PzMzb), which is distributed in a small area (~0.5 km²) south of the Murat River (Table 1, Figure 1c). It was stated that the base of the massif is composed of gneiss, metatuff-metavolcanic, and amphibolites, while the upper parts are composed of mica-schist, marble, marble-schist alternations (Erdoğan and Dora, 1983; Helvacı, 1983). On the other hand, Göncüoğlu and Turhan (1985) stated that Bitlis metamorphics made up of austere gneiss, garnet gneiss, biotite gneiss, amphibolite, quartzite, schist, marble, metatuff, calcschist, etc. This unit has a spread of ~0.29 % of the area (Table 1, Figure 1c).

The Guleman ophiolite (Kg), occurs in limited areas has a spread of ~0.39%, and consists of basic and ultrabasic rocks such as dunite, harzburgite, lerzolite, gabbro, pillow lava, and diabase. According to various researchers, the age of the unit is Late Cretaceous (Soytürk and Baştuğ, 1973), Jurassic (Açıkbaş and Baştuğ, 1975), and Cretaceous (Özkaya, 1978), Upper Toronian-Campanian (Herece, 2008).

The Yüksekova complex (Ky) covering ~49.48% of the study area includes volcano-sedimentary rocks

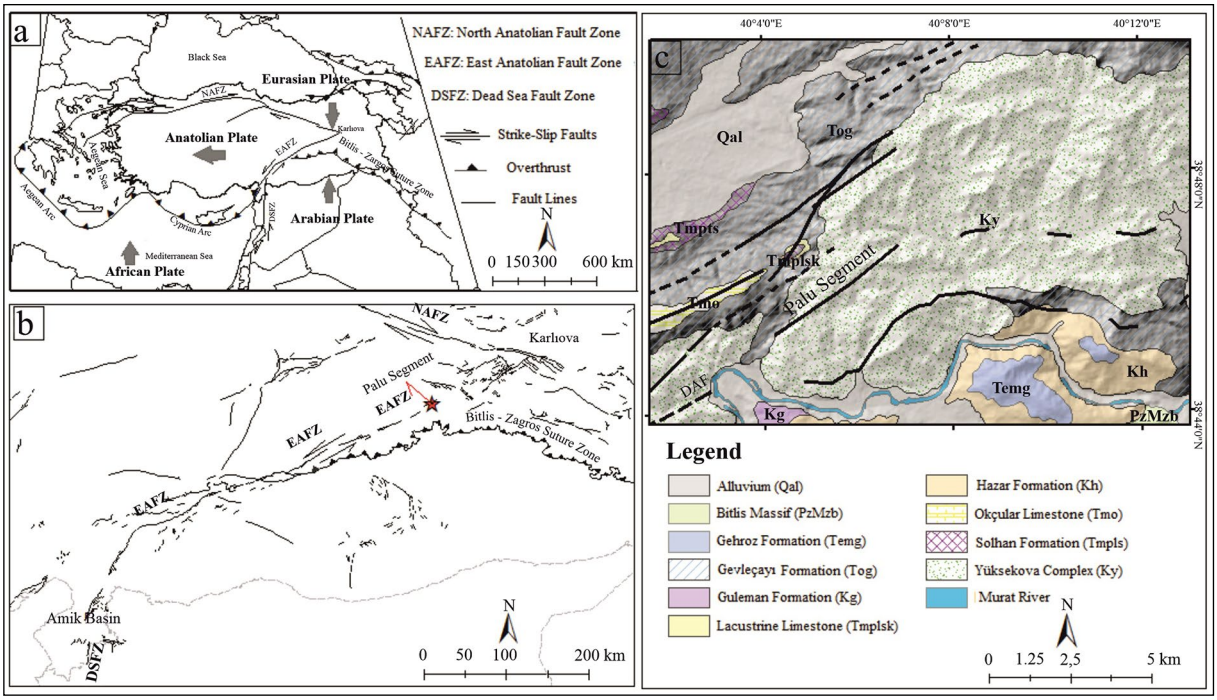

Figure 1- a) Simplified active tectonic scheme of Turkey (modified from Şaroğlu et al., 1992*a*; Emre et al., 2013); b) major branches of EAFZ (modified from Şaroğlu et al., 1992*b*; Herece, 2008); c) Geology of the Palu Segment of the EAFZ (modified from Sümengen, 2011).

(Table 1, Figure 1c). This unit was named by Perinçek (1979), and their age was accepted as Campanian-Early Maastrichtian. This unit consists of conglomerate, red-colored limestones, mudstones, sandstone, shale volcanic sandstone, tuff, agglomerate, basalt, spilite, pillow lava, diabase, and pelagic limestones (volcano-sedimentary unit), and basic and ultrabasic rocks such as serpentinite, granite, granodiorite, gabbro (Sümengen, 2011).

The Hazar formation (Kh), which makes up about 6.10% of the study area, contains alternations of gray shale, marl, sandstone, milstone, conglomerate, and clayey limestone (Table 1, Figure 1c). The unit starts with serpentinite and ultrabasic pebbly, grain-supported unsorted conglomerate at the bottom, and passes into conglomerate-sandstone and rudist-bearing packstone towards the top. The upper levels of the unit consist of alternations of gray, brownish shale, red fine-grained sandstone, siltstone and abundant-grained shell, gray, clayey limestone, and shale. Thin basalt levels are also present in the unit. Hazar formation overlies the Bitlis metamorphics, the Guleman ophiolites, and the Yüksekova complex with an angular unconformity (Sümengen, 2011). Based on fossils the age of the formation is Late Cretaceous (Ayhan, 1970).

The Gehroz formation (Temg) covers ~2% of the area (Table 1, Figure 1c). This formation starts with red sandstone and marl at the bottom and transitions to massive, beige, gray, fossiliferous micritic and biomicritic limestones towards the top, and is of Early-Middle Eocene age according to its fossil content (Özkaya, 1978).

The Gevleçayı formation (Tog), constitutes ~24.98% of the study area (Table 1, Figure 1c). It is composed of conglomerate, sandstone, claystone, sandy limestone, and algal clayey limestone (Metin, 1972; Sirel et al., 1975). The unit is deposited in a shallow marine environment. The section taken on the unit begins with a poorly sorted conglomerate level consisting of metamorphic, diorite, serpentinite, gabbro, and quartz pebbles at the base. It passes into sandstone-marl alternation towards the top. There are marly layers in the upper levels of the formation and between these are algal and clayey limestone layers. The age of the unit is thought to be Oligocene (Sümengen, 2011).

Okçular limestone (Tmo), is in the west of the study area and forms ~1% of the area (Table 1, Figure 1c). It consists of fine tuff intermediate, medium-thick bedded, white, gray colored algae, and clayey limestones rich in macro and microfossils. These units were named by Metin (1972). Based on the fossils the age of the formation is Early Miocene (Metin, 1972; Sirel et al., 1975).

Solhan formation (Tmpls), is found in limited areas in the study area and covers ~0.95% of the area (Table 1, Figure 1c). It consists of tuffite, basaltic andesite, pyroclastic intercalated lake sediments, tuffite-claystone intercalation, agglomerate, conglomerate, lamella branch, and lake sediments with gastropods. These sedimentary units are found in the formation as lenses with no lateral continuity. Lava consists of basalt, basaltic andesite, and andesitic basalt. The thickness of this unit varies between 20-30 meters in the region (Sümengen, 2011). Sirel et al. (1975) defined the volcanic unit in the area as Karadağ basalts. There are lacustrine limestones (Tmplsk) both below and above this unit and the age of the unit is accepted as Late Miocene-Pliocene (Sümengen, 2011). Alluvial (Qal) units, which make up about 14.49% of the research area, are the youngest of the area (Table 1, Figure 1c).

Table 1- The spatial and percentage distribution of units in the study area.

Name	Symbol	Area (Km^2)	%
Bitlis massif	PzMzb	0.56	0.29
Guleman formation	Kg	0.75	0.39
Yüksekova complex	Ky	96.06	4.48
Hazar formation	Kh	11.84	6.10
Gehroz formation	Temg	4.11	2.12
Gevleçayı formation	Tog	48.50	24.98
Okçular limestone	Tmo	1.91	0.98
Solhan formation	Tmpls	1.84	0.95
Lacustrine limestone	Tmplsk	0.45	0.23
Alluvium	Qal	28.13	14.49

3. Data and Data Preprocessing

3.1. ASTER Data Sets

The United States Geological Research Institution's (USGIS) spectral library data, ASTER images, geology, and fault maps are the key datasets utilized to analyze the relationship between mineral alteration and tectonic activity. The ASTER image dated 29.08.2004 was downloaded from the USGS website (https://earthexplorer.usgs.gov/) in hierarchical data format (HDF). Wavelength ranges and spatial resolutions of ASTER bands are given in Table 2.

Table 2- Description of the ASTER data.

Bands		Spectral Bandwidth (μm)	Spatial Resolution (m)
VNIR	Band-1	0.52-0.60	15
	Band-2	0.63-0.69	
	Band-3N	0.78-0.86	
	Band-3B	0.78-0.86	
SWIR	Band-4	1.60-1.70	30
	Band-5	2.145-2.185	
	Band-6	2.185-2.225	
	Band-7	2.235-2.285	
	Band-8	2.295-2.365	
	Band-9	2.360-2.430	
TIR	Band-10	8.125-8.475	90
	Band-11	8.475-8.825	
	Band-12	8.925-9.275	
	Band-13	10.25-10.95	
	Band-14	10.95-11.65	

The satellite images are in World Geodetic System 1984 (WGS 84) - Universal Transversal Mercator (UTM) Zone 37. In the study, sensor calibration of the image was conducted by converting Digital Numbers (DN) to Top of Atmosphere (TOA) reflectance values, following the methodology proposed by Abrams and Hook (1998). Equation 1 was used for the transformation at this stage.

$$\text{Radiance}=(\text{DN}-1)\ *\text{ucc} \quad (1)$$

Where DN is the digital number and ucc is the unit of conversion coefficient.

For each ASTER band, a distinct unit conversion coefficient applies. These numbers are taken from the ASTER user manual, Version 1 (Abrams and Hook, 1998). Then, to obtain in the VNIR-SWIR range with equal cell size, ASTER VNIR bands were resampled to 30 m. cell size and stacked with SWIR bands in ENVI 5.1 software environment. Then, the atmospheric correction algorithm Fast Line-of-sight Atmospheric Analysis of Hypercubes (FLAASH) () was applied. This algorithm is considered a first-class atmospheric correction tool that corrects VNIR through the NIR and SWIR regions up to 3 μm (ENVI, 2009).

After pre-processing the ASTER image, the water body and vegetated areas were masked from the image. In this process, water bodies were extracted from ASTER images using the Normalized Difference Water Index (NDWI) (Equation 2) (Gao, 1996), and vegetated areas were extracted using the Normalized Difference Vegetation Index (NDVI) (Equation 3) Kriegler et al., 1969).

$$\text{NDWI} = (\text{NIR}-\text{SWIR})/(\text{NIR}+\text{SWIR}) \quad (2)$$

$$\text{NDVI} = (\text{NIR}-\text{R})/(\text{NIR}+\text{R}) \quad (3)$$

3.2. Spectral Library Data

The spectral library comprises reflections of target objects recorded in both field and laboratory settings using radiometers. Mineral spectra have a prominent place in spectral libraries. In the study, spectral reflectances of minerals, obtained from the USGS spectral library (http://speclab.cr.usgs.gov/spectral.lib04/spectral_lib.html), were utilized. The minerals used are goethite, hematite, jarosite, limonite, alunite, epidote, illite, kaolinite, montmorillonite, and muscovite (Table 3). These minerals were extracted from the USGS library file and resampled to match the spectral range of the bands of the ASTER image.

Rocks and minerals have a higher reflectance value in the SWIR region than in the VNIR region, so the 6 band of the ASTER satellite, which is in the wavelength range of 1.60 to 2.430 (μm), is appropriate for identifying hydrothermal alteration minerals. The absorption properties of iron minerals such as jarosite, limonite, hematite, and goethite are especially related to Fe_3+and Fe_2+The absorption properties of Fe_3+is about 0.49, 0.70, and 0.87 μm, while the absorption property of Fe_2+is about 0.51, 0.55, and 1.20 μm. The absorption properties of Fe_3+are approximately 0.49,

Table 3- The USGS spectral library's minerals used and their codes (http://speclab.cr.usgs.gov/spectral.lib04/spectral_lib.html).

Minerals	Codes
goethit1.spc	Goethite WS222
hematit2.spc	Hematite GDS27
jarosit1.spc	Jarosite GDS99 K-y 200C
limonite. spc	Limonite HS41.3
alunite1.spc	Alunit GDS84 $Na0_3$
epidote1.spc	Epidote GDS26.a 75-200um
illite1.spc	Illite GDS4 (Marblehead)
kaolini1.spc	Kaolinite CM9
montmor1.spc	Montmorillonite SWy-1
Muscovi2.spc	Muscovite GDS108

0.70, and 0.87 µm, while the absorption properties of Fe_2+ are approximately 0.51, 0.55, and 1.20 µm (Figure 2). That is, in the visible and mid-infrared wavelength ranges, these minerals tend to show strong spectral reflection-absorption properties (Hunt and Salisbury, 1974; Hunt, 1977; Hunt and Ashley, 1979; Cloutis, 1996; Rowan et al., 2006; Mars and Rowan, 2011; Fatima et al., 2017). Al-Si-(OH) and mg-Si-(OH) bearing minerals like montmorillonite, kaolinite, muscovite, illite, chlorite, and talc and Ca-Al-Si-(OH) bearing minerals like sorosilicate group, epidote group, and alunite phyllosilicates, including OH-bearing sulfates, as well as carbonates can be recognized by their spectral reflection properties in the shortwave infrared regions (Hunt, 1977; Hunt and Ashley, 1979; Amin and Mazlan, 2011; El Janati, 2019). Clay minerals such as alunite, kaolinite, and montmorillonite show high reflectance at 1.6 µm. However, they show intense absorption in the 2.1-2.4 µm wavelength range (Hunt and Ashley, 1979; Figure 2).

3.3. Faults and Geological Maps

The faults of the study area were compiled from maps of different scales provided by the Mineral Research and Exploration General Directorate (MTA). 1:250.000 scale digital faults map in pdf format was downloaded from the Mineral Research and Exploration General Directorate website (www.mta.gov.tr) to gain a comprehensive understanding of the tectonic features of the region. Turkey Geology K44 map of the study area at 1/100.000 scale was obtained from Mineral Research and Exploration General Directorate (MTA) with the necessary correspondence. Also, 1/100.000 scaled Atlas of East Anatolian Fault (Herece, 2008) was used in the study.

4. Methods

4.1. Band Ratio, Relative Band Depth (RBD), and Mineral Indices

The Band Ratio technique was developed based on the principle that an object with high reflection in a certain wavelength range of the EMS gives low reflection in another wavelength range. This method detects alterations by dividing the wavelength range with high reflection by the wavelength range with low reflection. Thus, features that cannot be differentiated in a single band are highlighted by emphasizing the spectral differences between materials due to band

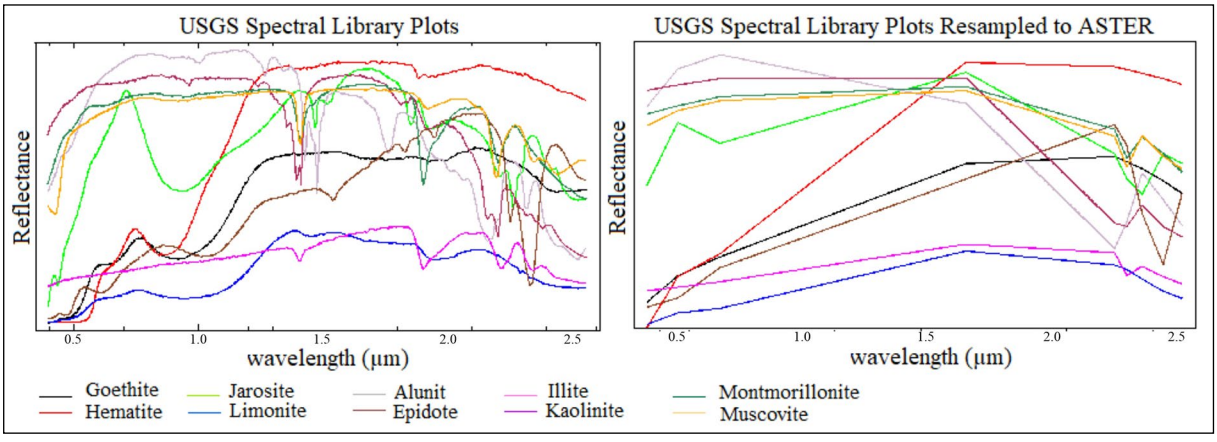

Figure 2- Mineral spectra from the USGS library and resampling of these reflections to ASTER satellite bands.

rationing. In addition, this method also contributes to highlighting the target material in the image by reducing the shadow effect caused by solar illumination and topography (Holben and Justice, 1981; Sabins, 1999; Kayadibi, 2008). In the study, band ratio values widely accepted in the literature were considered to determine the alterations of ferric oxide, gossan, alunite, iron oxide, amphibole, kaolinite, calcite, and kaolinite-montmorillonite minerals (Table 4).

Relative Band Depth (RBD) was proposed by Crowley et al. (1989) to detect diagnostic mineral absorption properties. This method is based on the band rationing principle and, like this method, minimizes reflection variations related to slope and albedo differences in topography. The total of many data channels near an absorption band is divided by the sum of numerous channels near the minimum band to produce an RBD image. RBD images are too sensitive to the presence of certain mineral absorption properties besides extremely specific. Furthermore, spectral features that arise when using other data normalization techniques are neither modified nor suppressed with the methodology. The RBD technique is particularly well suited for detecting weak NIR spectral features produced by soils, allowing better mapping of fine lithological and structural details in semi-arid terrains (Crowley et al., 1989). In the study, RBD ratios widely accepted in the literature were used to determine alterations of amphibolites, dolomite, carbonate-chlorite-epidote, alunite-pyrophyllite, alunite-pyrophyllite-kaolinite, kaolinite-montmorillonite, ilite-smectite-muscovite minerals (Table 4).

Compared with the band ratios, mineral indices provide a contrast difference between materials by taking advantage of the electromagnetic energy difference between the absorption and reflection bands. The difference between band indices and band ratios is expressed by multiplying or adding two different band ratios. The logic behind combining two distinct band ratios is to enhance differentiation among materials that exhibit similar spectral reflectance characteristics.

Table 4- ASTER Band Ratio, Relative Band Depth (RBD), and Mineral Indices employed for the identification of alteration minerals.

Methods	Minerals	Band Ratios	References
Band Ratios	Ferric Oxide	(Band 4 / Band 3)	Hewson et al., 2001
	Gossan	(Band 4 / Band 2)	Volesky et al., 2003
	Alunite	(Band 4 / Band 5)	Rouskov et al., 2005
	Iron Oxide	(Band 2 / Band 1)	Hewson et al., 2001
	Amphibole	(Band 6 / Band 8)	Hewson et al., 2005
	Kaolinite	(Band 7 / Band 5)	Hewson et al., 2005
	Kaolinite	(Band 7 / Band 6)	Van der Meer et al., 2014
	Calcite	(Band 4 / Band 7)	Rouskov et al., 2005
	Kaolinite-Montmorillonite	(Band 4 / Band 6)	Rouskov et al., 2005
RDB	Amphibolites	(Band 6+Band9) / (Band 8)	Hewson et al., 2005
	Dolomite	(Band 6+Band8) / (Band 7)	Rowan and Mars, 2003
	Carbonate-Chlorite-Epidote	(Band 7+Band9) / (Band 8)	Rowan and Mars, 2003
	Alunite-Pyrophyllite	(Band 6+Band7) / (Band 5)	--
	Alunite-Pyrophyllite-Kaolinite	(Band 4+Band6) / (Band 5)	Rowan and Mars, 2003
	Kaolinite-Montmorillonite	(Band 4+Band7) / (Band 6)	Fatima et al., 2017
	Illite-Smectite-Muscovite	(Band 5+Band7) / (Band 6)	Rowan and Mars, 2003
Mineral Indices	OH	(Band 7/ Band 6) * (Band 4/ Band 6)	Ninomiya, 2004
	Kaolinite	(Band 4/b 5) * (Band 8/Band 6)	Ninomiya, 2004
	Alunite	(Band 7/b 5) * (Band 7/Band 8)	Ninomiya, 2004
	Calcite	(Band 6/ Band 8) * (Band 9/Band 8)	Ninomiya, 2004
	Iron	(Band 2/Band 1) * (Band 3/Band 2)	Gopinathan et al., 2020
	Ferrus Iron	(Band 1+ Band 4) / (Band 2/Band 3)	Rockwell, 2013

The Mineral Index is formulated by selecting one absorption band and two reflection bands. In this study, Table 4 lists the band indices recognized in the literature for identifying alterations associated with OH, kaolinite, alunite, calcite, iron, and ferrous iron minerals.

4.2. Crosta

Crosta and Moore (1989) applied a different approach to Principal Component Analysis (PCA), which they defined as feature-orientated principal component selection (FPCS), in their work. Later, this approach was introduced into the literature by Loughlin (1991) as the CROSTA technique and has been applied to various satellite images to detect hydrothermal alteration minerals in ongoing investigations (Loughlin, 1991; Tangestani and Moore, 2002).

Using this strategy, the user selects 4 or 6 spectral bands according to the spectral reflectance of the objects. In the band selection, the band gap of the target mineral with the highest reflectance and the lowest reflection is selected and PCA is applied to these selected bands. For this reason, the most crucial point to be considered while performing the CROSTA analysis is the correct band selection. When the obtained PCs are examined, it is seen that the absorption bands of the mineral gave a brighter image with positive values, while the desorption bands gave a darker image with negative values.

4.3. Constrained Energy Minimization (CEM)

The Constrained Energy Minimization (CEM) technique was developed by Harsanyi (1993). This technique is a quick and efficient way to increase the reflections of the desired object while decreasing the effects of undesirable objects in the data, namely their spectral reflections. All that is required for this technique is the spectra of the desired target, which is the spectra of the minerals for this study. CEM allows us to highlight the signature of interest while minimizing unwanted, and unknown background signatures of each pixel in the multispectral image sequence. Using a Finite Pulse Response (FIR) filter, the CEM method linearly limits a targeted object while minimizing interference from other unidentified signal sources. The CEM technique's capacity to manage a variety of spectral backgrounds and accept nonlinear blends of background elements is among its advantages (Farrand and Harsanyi, 1997). Researchers have demonstrated that this method effectively isolates the target signature from satellite images (Zhang et al., 2007; Gabr et al., 2010; Li et al., 2014; Guha et al., 2014; Pour et al., 2017, 2019).

4.4. Mixed Tuned Matched Filter (MTMF)

The Mixed Tuned Matched Filtering (MTMF) technique is a sub-pixel mapping method that comprises a combination of the Linear Spectral Mixed and the Statistical Matched Filtering (MF) techniques (Boardman et al., 1995). However, in addition to a feasibility index gives more weight to the output of each end-member and results in an improved technique that can detect small spectrum changes and signal the most favorable locations. The MTMF consists of two phases: an MF calculation for estimating abundance and a mix adjustment calculation for identifying and rejecting false positives. The outcomes of the MTMF give two sets of gray images for each target, containing the MF image score and the feasibility image. With values ranging from 0 to 1.0, the MF image leads a way to assess the degree of similarity to the reference spectrum and the approximate subpixel abundance. In the MF technique, the feasibility perspective is occasionally employed to mitigate false positives by integrating the physical constraints of mixture theory with the advantages of matched filtering. The mixture-tuned technique utilizes linear mixed-spectrum theory to constrain the feasibility of mixed outcomes and thereby reduce the occurrence of false signals (Wang and Zhang, 2011).

4.5. Getis–Ord Gi* Statistics

Getis-Ord Gi* statistics is a local spatial autocorrelation index (Getis and Ord, 1992; Ord and Getis, 1995). This statistic is suitable for identifying a group of features in the entire study region that occurs within a specified distance and has a high or low concentration. The Gi* statistic yields a z-score and p-values for each feature in the dataset, indicating spatial clusters of high or low attribute values. The clustering of high attribute values (hot spot) is shown by statistically significant positive z-scores. However,

the clustering of low attribute values is shown by statistically significant negative z-scores (cold spot). Gi* is the spatial autocorrelation statistic of an event I over n occurrences, and it is determined using Equation (4):

$$G_i^* \frac{\sum_{j=1} W_{ij} x_j}{\sum_{j=1} x_j} \quad (4)$$

where xj describes the attribute value of feature j, Wij is the spatial weight between the feature I and j, and Gi* is the spatial autocorrelation statistic of an event I over n events.

5. Discussions

Active tectonics can significantly influence mineral alterations by creating conditions conducive to hydrothermal processes and deformation. Tectonic activities such as faulting, folding, and uplift can introduce fluids into the Earth's crust, facilitating the alteration of minerals through processes such as metasomatism and hydrothermal replacement. Fault zones, in particular, act as pathways for fluid migration, which can induce chemical reactions leading to the formation of new minerals or the alteration of existing ones. Moreover, the intensity and frequency of seismic activity associated with active tectonics can contribute to the fracturing and shearing of rocks, further promoting mineral alterations. This relationship underscores the importance of considering tectonic settings and associated geological structures when studying mineral alterations and their spatial distribution in geological contexts.

In the study, to determine the relationship between active tectonics and mineral alterations, Band Ratio, RBD, Mineral Indices, CROSTA, CEM, and MTMF algorithms were applied to the ASTER data to map the alteration minerals at the pixel level. The analysis of the Band Ratio identified that kaolinite (28.23%) and ferric oxide (17.50%) constitute the highest percentages of minerals in the region, whereas gossan (1.46%) and alunite (4.03%) represent the lowest percentages. (Table 5). Rockwell (2013) states that automated ASTER data processing techniques provide outcomes for individual material indices using ratio-based spectral analysis programs. The high-end values of an index will be displayed as a detection result even if there are no minerals of the type it was intended to highlight in the scene. As a result, the maps produced by ratio-based analysis algorithms are those with a high likelihood of containing a certain item. Since the mineral groups determined by band ratio in this study are quite common in the study area, no significant incorrect mineral group detections related to the algorithm itself were observed in the tests performed for this study. According to the results, kaolinite alterations are widely distributed in the Yüksekova complex (Ky), especially in the northeastern part of the complex and around the Murat River. On the other hand, intense amphibolite alterations are limited to the fault lines at the northeast and southwest ends of the Palu fault segment. Ferric oxide and iron oxide alterations dispersed along the fault line and in the immediate vicinity (Figure 3a1). According to findings

Table 5- Mineral alterations and their respective percentage distributions derived from Band Ratio, RBD, and Mineral Indices analyses.

Methods	Minerals	%	Minerals	%
Band Ratios	Ferric oxide	17.50	Amphibolites	17.37
	Gossan	1.46	Kaolinite	28.23
	Alunite	3.03	Calcite	8.60
	Ferric oxides	20.78	Kaolinite-Montmorillonite	3.03
RDB	İlit-Smektit-Muskovit	13.14	Carbonate- chlorite-epidote	6.29
	Kaolinite-montmorillonite	6.84	Dolomite	19.70
	Alunite-Pyrophyllite-Kaolinite	12.76	Amphibolites	18.84
	Alunite-pyrophyllite	22.41		
Mineral Indices	OH	6.52	Alunite	14,75
	Kaolinite	9.99	Ferrus iron	47.26
	Calcite	21.48		

of the Getis–Ord Gi* statistics at the 99 and 95% confidence intervals the clustering of the cold spots indicating closeness to the faults, are more intensely clustered around the fault lines and parallel to the fault lines. On the other hand, at the same confidence intervals, statistically significant hot spot (positive z-scores) values are clustered independently from the fault lines (Figure 3a2).

Based on the findings of the RDB analysis, the area exhibits the highest percentages of alunite-pyrophyllite (22.41%), dolomite (19.70%), and amphibolite's (18.84%), whereas kaolinite-montmorillonite (6.84%) and carbonate-chlorite-epidote (6.29%) minerals show the lowest percentages. Dolomite alterations are prevalent throughout the area, with amphibole alterations observed intermittently, particularly concentrated around fault lines and aligned parallel to their extensions (Figure 3b1). According to the results of the Getis–Ord Gi* statistics at the 99% and 95% confidence intervals, findings were consistent with those obtained from band ratio analyses (Figure 3b2).

The findings of the Mineral Indices indicate ferrous iron (47.26%), and calcite (21.48%) alterations are the most common in the area (Table 5). Based on the spatial pattern of mineral alterations, calcite modifications predominantly cluster in the northeastern and southwestern sectors of the Palu fault segment. Ferrus iron alterations are observed proximal to the fault lines and align parallel to their extension (Figure 3c1). The results of the Getis–Ord Gi* statistics at the 99% and 95% confidence intervals indicate that cold spot clusters are predominantly located along the fault lines and in their immediate vicinity, consistent with the findings from Band Ratio and RBD analyses (Figure 3c2).

In the study area, alunite, kaolinite, muscovite-sericite, and ferric oxide alterations were identified using the CROSTA method. In this analysis, the selected ASTER bands (Crosta et al., 2003; Boloki and Poormirzaee, 2010) to determine each mineral alteration are given in Table 6.

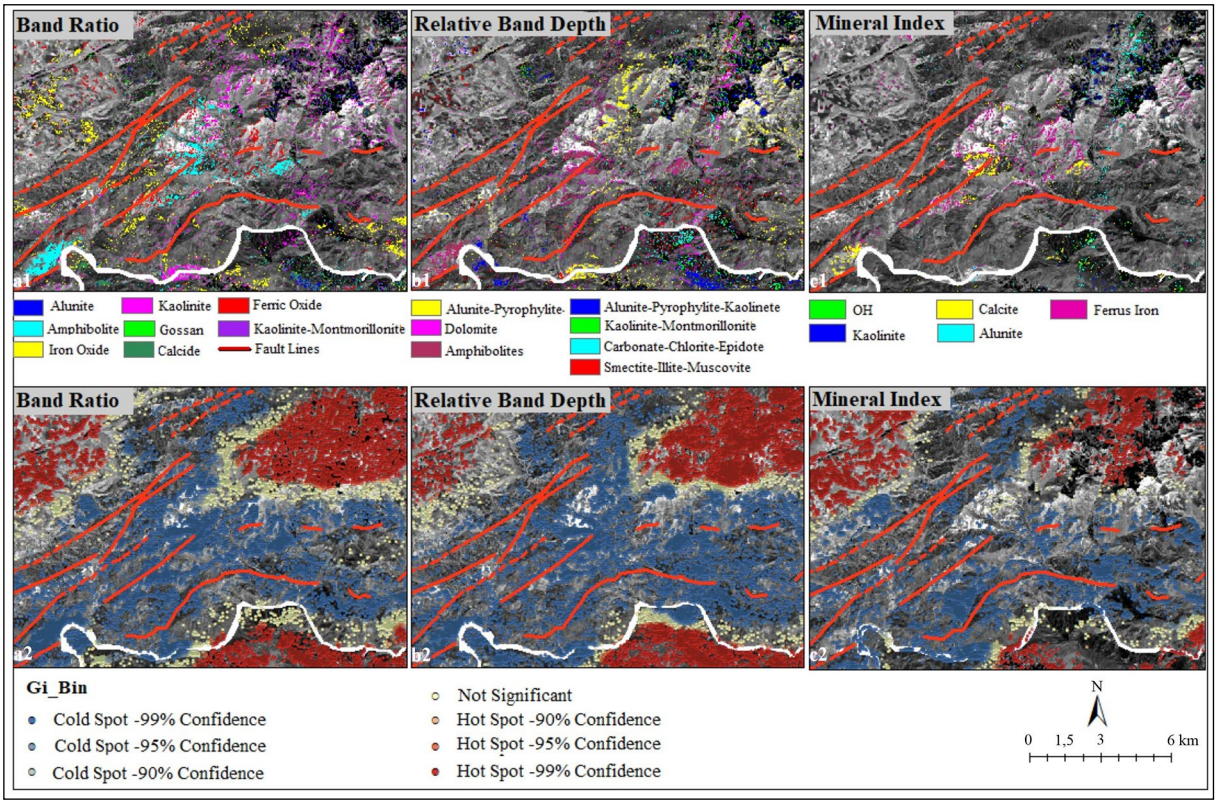

Figure 3- Alteration minerals determined by Band Ratio (a1), RBD (b1) and Mineral Indices (c1) and results of the Getis–Ord Gi* statistics of these alterations according to fault lines (a2; b2; c2, respectively).

Table 6- The ASTER bands selected to detect alteration minerals in the CROSTA method.

CROSTA Bands	Minerals	References
B1-B3-B5-B7	Alunite	Crosta et al., 2003
B1-B4-B6-B7	Kaolinite	Crosta et al., 2003
B1-B3-B5-B6	Muscovite&sericite	Crosta et al., 2003
B1-B2-B3-B4	Ferric oxides	Boloki and Poormirzaee, 2010

After selecting the necessary 4 bands for each alteration, PCA analysis was conducted on these bands. Eigenvector values of each PC obtained from this analysis are given in Table 7. The eigenvalues provided in the table are crucial for the principal components analysis (PCA), which is essential for identifying minerals such as alunite, kaolinite, muscovite-sericite, and ferric oxide. According to the eigenvector values, PC 4 is considered most suitable for identifying alunite, kaolinite, muscovite-sericite, and ferric oxides. In this component, the identification of mineral types reveals distinct spectral signatures across various bands. Specifically, for alunite minerals, the spectral reflectance ranges from a minimum value observed in Band 5 (-0.638) to a maximum in Band 7 (0.729). For kaolinite minerals, the spectral reflectance varies from its lowest in Band 6 (-0.695) to its highest in Band 7 (0.718). Muscovite-sericite minerals exhibit spectral reflectance values ranging from a minimum in Band 3 (-0.023) to a maximum in Band 7 (-0.698). Finally, for ferric oxides, spectral reflectance ranges from a minimum observed in Band 3 (-0.682) to a maximum in Band 1 (0.719).

Table 7- Eigenvectors of alunite, kaolinite, muscovite and sericite, and ferric oxides for selected ASTER bands (PCA for 4 bands).

Eigenvectors-Alunite	B1	B3	B5	B7
PC 1	-0.485	-0.562	-0.469	-0.475
PC 2	-0.399	0.823	-0.300	-0.268
PC 3	0.777	0.070	-0.470	-0.411
PC 4	-0.025	-0.024	-0.683	0.729
Eigenvectors-Kaolinite	B1	B4	B6	B7
PC 1	-0.447	-0.595	-0.486	-0.455
PC 2	-0.832	0.549	0.063	0.030
PC 3	0.326	0.584	-0.524	-0.525
PC 4	-0.009	0.026	-0.695	0.718
Eigenvectors-Muscovite and Sericite	B1	B3	B5	B6
PC 1	-0.479	-0.544	-0.468	-0.504
PC 2	-0.377	0.835	-0.289	-0.273
PC 3	0.791	0.068	-0.430	-0.427
PC 4	-0.009	-0.023	0.715	-0.698
Eigenvectors- Ferric oxides	B1	B3	B5	B6
PC 1	0.414	0.545	0.475	0.551
PC 2	0.448	0.440	-0.770	-0.106
PC 3	-0.330	-0.206	-0.423	0.817
PC 4	0.719	-0.682	0.011	0.123

The rule-based classification methods were then used to map modifications after selecting the PCs needed to determine the alteration minerals alunite, kaolinite, iron oxide, muscovite and sericite (Figures 4a1, b1, c1, d1 respectively). In the CROSTA method, by selecting the bands with the highest and lowest spectral reflections for each mineral and reducing the number of bands, the chance of identifying a unique PC for a particular mineral class increased as mentioned in Loughlin (1991). According to the findings of the CROSTA analysis, occurrences of alunite, kaolinite, iron-oxide, and muscovite-sericite alterations were predominantly noted in the northeastern, southern, and central parts of the study area. Considering the results of the Getis–Ord Gi* statistics at the 99 and 95% confidence intervals, cold spot values are mainly distributed along the fault lines and limited by the fault lines. On the other hand, especially alunite and kaolinite hot spot values are clustered in the northeastern part of the area. Notably, alunite and kaolinite hot spot values are more densely clustered in the northeast part of the area concerning Iron-oxide and muscovite sericite hot spot values (Figures 4a2, b2, c2, d2).

The CEM method was applied to the VNIR and SWIR regions of the ASTER data. With this method hematite, goethite, jarosite, and limonite minerals were determined in the VNIR region (Figures 5a1, 5a2). On the other hand, alunite, kaolinite, montmorillonite illite, muscovite, and epidote minerals were determined in the SWIR region. According to the results obtained, limonite and illite alterations detected in the northwestern parts of the area are limited by fault lines in places. On the other hand, epidote alterations are intensely present on the fault surroundings extending along the northeast of the study area and limited by faults. Considering the results of the Getis–Ord Gi* statistics at the 99 and 95% confidence intervals cold spot values are mainly

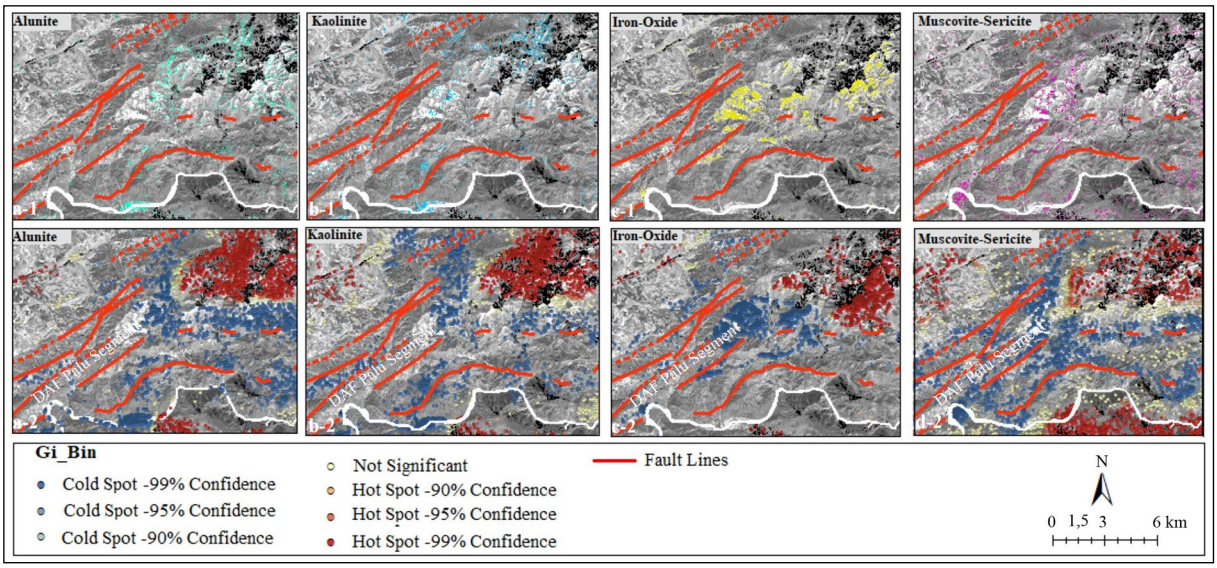

Figure 4- Alteration minerals determined by CROSTA analysis (a1, b1, c1, d1) and results of the Getis–Ord Gi* statistics of these alterations according to fault lines (a2, b2, c2, d2).

dispersed along the fault lines and limited by the fault lines (Figure 5a3).

The MTMF technique was applied to the ASTER VNIR and SWIR bands according to the reflection spectrum of the minerals of interest selected from the spectral library. According to the VNIR wavelength range results of the MTMF, limonite alteration clustered in some areas was detected on the fault line in the southern part of the study area and in its

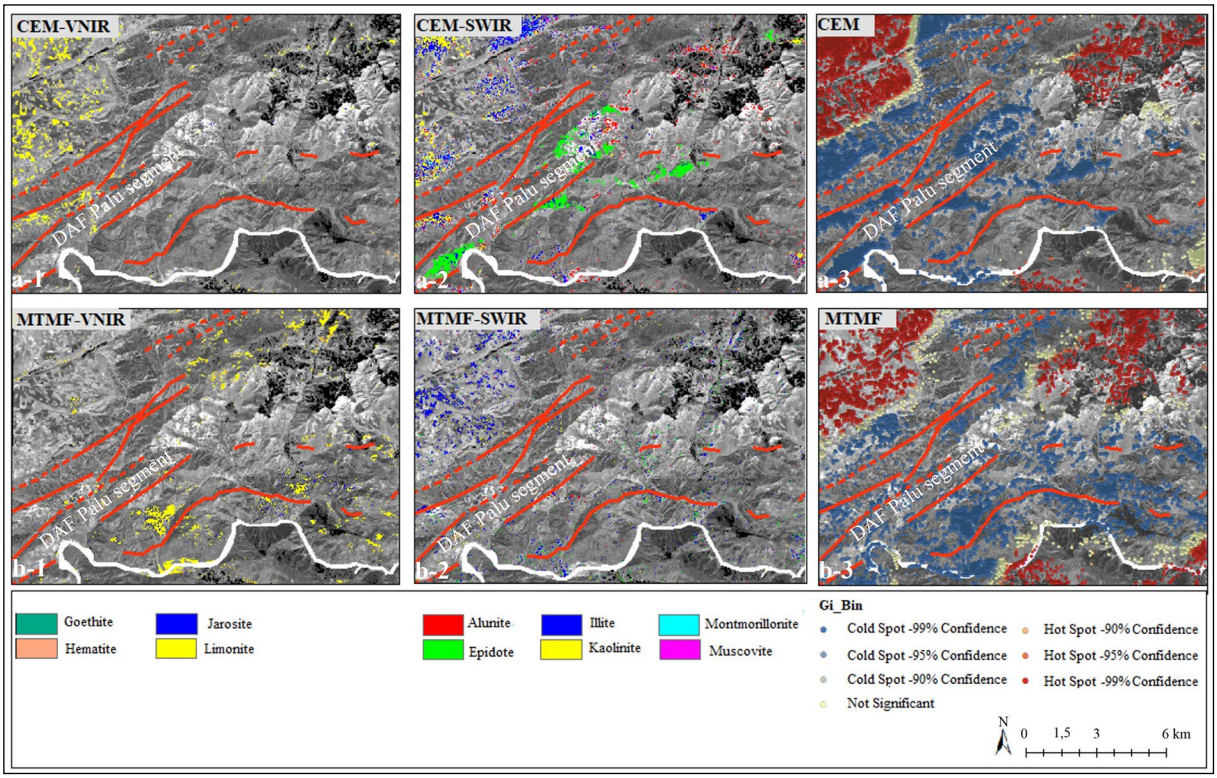

Figure 5- Alteration minerals determined by CEM and MTMF analyses applied to the ASTER VNIR (a1, b1) and SWIR (a2, b2) bands, respectively. The Getis–Ord Gi* statistics of these alterations resulting CEM (a3) and MTMF (b3).

immediate vicinity. On the other hand, in the SWIR region, illite alterations were observed northwest part of the area like the results of the CEM (Figures 5b1, 5b2). When the Getis–Ord Gi* statistics at the 99 and 95% confidence intervals of these mineral alterations are examined, the distribution of cold spot clusters was mainly placed parallel to the extension of the fault lines and limited with the fault lines (Figure 5b3).

According to the visual and spatial comparisons of the mineral alterations determined at the pixel level, it was determined that the distributions of the alteration minerals determined from the ASTER data were mostly consistent. This result, in a way, indicates the accuracy of the analysis results of the applied methods. The good correlation of the alteration minerals results with each other near the fault lines also proved the consistency of these applied methods. In addition, in the mineral alterations detected along the fault lines, left lateral offsets were observed in some places, consistent with the general character of the fault system. It is thought that mineral alterations concentrated on active fault lines will also contribute to determining fault lines that cannot be resolved with field studies.

6. Conclusion

The spatial distribution of alteration minerals, which extends in a manner parallel to tectonically active fault lines and is influenced by fault boundaries within the area, provides valuable insights into the spatial interplay between tectonic activity and the processes of mineral alteration. Through the utilization of RBD, Mineral Indices, CROSTA, CEM, and MTMF image processing algorithms, the study consistently achieved accurate spatial identification and mapping of mineral alterations across the entire study area. Statistical validation through Getis-Ord Gi* statistics further supports the reliability and consistency of these spatial patterns.

The observed displacements along fault lines, especially in active tectonic zones, significantly enhance the rates of mineral alteration processes. The alignment of alteration mineral distributions in specific areas parallel to the orientation of active fault lines suggests the existence of underlying fault characteristics even in regions where faults are not visibly apparent. This spatial relationship underscores the study's significance by providing foundational insights to geoscientists before conducting field investigations. Moreover, these findings serve as critical spatial indicators for on-site identification and mapping of fault systems, thereby contributing to a deeper understanding of the geological dynamics influencing mineral alteration processes.

References

Abrams, M., Hook, S. J. 1995. Simulated ASTER data for geologic studies. IEEE Transactions on Geoscience and remote sensing, 33 (3), 692-699.

Abrams, M., Hook, S. 1998. ASTER user handbook, version 1, NASA/Jet Propulsion Laboratory, Pasadena.

Açıkbaş, D., Baştuğ, C. 1975. V. Bölge Cacas-Hani yöresi kuzey sahalarının jeoloji raporu ve petrol olanakları. TPAO, Rapor No: 917, 45.

Amin, B., Mazlan, H. 2011. The Earth Observing-1 (EO-1) Satellite Data For Geological Mapping, Southeastern Segment of The Central Iranian Volcanic Belt, Iran. International Journal of Physical Sciences, 6 (33): 7638-7650.

Arpat, E. 1972. The East Anatolian fault system: thoughts on its development. MTA Bull., 78, 33-39.

Arpat, E., Şaroğlu, F. 1972. Doğu Anadolu Fayı İle İlgili Bazı Gözlem ve Düşünceler. Maden Tetkik ve Arama Dergisi 73, 1-9.

Ayhan, A. 1970. Elazığ K44-d2 Paftasının Jeolojisi. Elazığ Bingöl Diyarbakır İlleri Arasında Yer Alan Akdağların Jeolojisi. Maden Tetkik ve Arama Genel Müdürlüğü Rapor No: 93, Ankara (unpublished).

Barka, A. A., Kadinsky-Cade, K. 1988. Strike-slip fault geometry in Turkey and its influence on earthquake activity. Tectonics, 7 (3), 663-684.

Bayrak, E., Yılmaz, Ş., Softa, M., Türker, T., Bayrak, Y. 2015. Earthquake hazard analysis for East Anatolian fault zone, Turkey. Natural Hazards, 76, 1063-1077.

Boardman, J. W., Kruse, F. A., Green, R. O. 1995. Mapping target signatures via partial unmixing of AVIRIS data. In Summaries of the fifth annual JPL airborne earth science workshop, Volume 1: AVIRIS workshop.

Boloki, M., Poormirzaee, M. 2010. Using ASTER image processing for hydrothermal alteration and key alteration minerals mapping. Journal of Latest Trends on Engineering Mechanics, Structures, Engineering Geology, 1, 77-82.

Çetin, H., Güneyli, H., Mayer, L. 2003. Paleoseismology of the Palu–Lake Hazar segment of the East Anatolian fault zone, Turkey. Tectonophysics, 374 (3-4), 163-197.

Clark, R. N., King, T. V., Klejwa, M., Swayze, G. A., Vergo, N. 1990. High spectral resolution reflectance spectroscopy of minerals. Journal of Geophysical Research: Solid Earth, 95 (B8), 12653-12680.

Cloutis, E. A. 1996. Review article hyperspectral geological remote sensing: evaluation of analytical techniques. International Journal of Remote Sensing, 17 (12), 2215-2242.

Crosta, A. P., Moore, J. M. 1989. Geological mapping using Landsat thematic mapper imagery in Almeria Province, South-east Spain. International Journal of Remote Sensing, 10 (3), 505-514.

Crosta, A. P., De Souza Filho, C. R., Azevedo, F., Brodie, C. 2003. Targeting key alteration minerals in epithermal deposits in Patagonia, Argentina, using ASTER imagery and principal component analysis. International journal of Remote sensing, 24 (21), 4233-4240.

Crowley, J. K., Brickey, D. W., Rowan, L. C. 1989. Airborne imaging spectrometer data of the Ruby Mountains, Montana: Mineral discrimination using relative absorption band-depth images. Remote Sensing of Environment, 29 (2), 121-134.

Crowley, J. K. 1993. Mapping playa evaporite minerals with AVIRIS data: A first report from Death Valley, California. Remote Sensing of Environment, 44 (2-3), 337-356.

Dewey, J. F., Hempton, M. R., Kidd, W. S. F., Şaroğlu, F., Şengör, A. M. C. 1986. Shortening of continental lithosphere: The neotectonics of Eastern Anatolia—a young collision zone. Geological Society, London, Special Publications, 19 (1), 1-36.

Duman, T. Y., Emre, Ö., Özalp, S., Elmacı, H., Olgun, Ş. 2012. 1:250.000 Ölçekli Türkiye Diri Fay Haritası Serisi, Elazığ (NJ 37-7) Paftası, Seri No:45, Maden Tetkik ve Arama Genel Müdürlüğü, Ankara –Türkiye.

Duman, T. Y., Emre, Ö. 2013. The East Anatolian Fault: Geometry, segmentation and jog characteristics. Geological Society, London, Special Publications, 372 (1), 495-529.

El Janati, M. 2019. Application of remotely sensed ASTER data in detecting alteration hosting Cu, Ag and Au bearing mineralized zones in Taghdout area, Central Anti-Atlas of Morocco. Journal of African Earth Sciences, 151, 95-106.

Emre, Ö., Duman, T. Y. 2007. The East Anatolian Fault: Structural pattern and relationship with the Dead Sea Transform. In AGU Fall Meeting Abstracts, Vol. 2007, T42B-01.

Emre, Ö., Duman T. Y., Özalp, S., Elmacı, H., Olgun, Ş., Şaroğlu, F. 2013. Active fault map of Turkey with an explanatory text 1: 1,250,000 scale. General Directorate of Mineral Research and Exploration, special publication series, 30:89.

ENVI. ENVI EX User's Guide. 2009. http://www.harrisgeospatial.com/portals/0/pdfs/enviex/ENVI_EX_User_Guide.pdf.

Erdoğan, B., Dora O. Ö. 1983. Bitlis masifi apatitli demir yataklarının jeolojisi ve oluşumu. Türkiye Jeoloji Kurumu Bülteni. 26:133-44.

Farrand, W. H., Harsanyi, J. C. 1997. Mapping the distribution of mine tailings in the Coeur d'Alene River Valley, Idaho, through the use of a constrained energy minimization technique. Remote Sensing of Environment, 59 (1), 64-76.

Fatima, K., Khan Khattak, M. U., Kausar, A. B., Toqeer, M., Haider, N., Rehman, A. U. 2017. Minerals identification and mapping using ASTER satellite image. Journal of Applied Remote Sensing, 11 (4), 046006-046006.

Gabr, S., Ghulam, A., Kusky, T. 2010. Detecting areas of high-potential gold mineralization using ASTER data. Ore Geology Reviews, 38 (1-2), 59-69.

Gao, B. C. 1996. NDWI—A normalized difference water index for remote sensing of vegetation liquid water from space. Remote sensing of environment, 58(3), 257-266.

Getis, A., Ord, J. K. 1992. The analysis of spatial association by use of distance statistics. Geographical analysis, 24 (3), 189-206.

Göncüoğlu, M. C., Turhan, N. 1985. Bitlis metamorfik kuşağının orta bölümünün temel jeolojisi. Maden Tetkik ve Arama Genel Müdürlüğü Rapor No: 7707.

Gopinathan, P., Parthiban, S., Magendran, T., Al-Quraishi, A. M. F., Singh, A. K., Singh, P. K. 2020. Mapping of ferric (Fe^{3+}) and ferrous (Fe^{2+}) iron oxides distribution using band ratio techniques with ASTER data and geochemistry of Kanjamalai and Godumalai, Tamil Nadu, south India. Remote Sensing Applications: Society and Environment, 18, 100306.

Guha, A., Kumar, K. V., Rao, E. D., Parveen, R. 2014. An image processing approach for converging ASTER-derived spectral maps for mapping Kolhan limestone, Jharkhand, India. Current Science, 40-49.

Gülerce, Z., Tanvir Shah, S., Menekşe, A., Arda Özacar, A., Kaymakcı, N., Önder Çetin, K. 2017.

Probabilistic seismic-hazard assessment for East Anatolian fault zone using planar fault source models. Bulletin of the Seismological Society of America, 107 (5), 2353-2366.

Güvercin, S. E., Karabulut, H., Konca, A. Ö., Doğan, U., Ergintav, S. 2022. Active seismotectonics of the East Anatolian fault. Geophysical Journal International, 230 (1), 50-69.

Güzel, F. 2023. Uzaktan Algılama Teknolojileri Kullanarak Aktif Tektonik İle Mineral Alterasyonu Arasındaki İlişkinin Belirlenmesi. The Graduate School of Social Sciences of Süleyman Demirel University (In Turkish).

Harsanyi, J. C. 1993. Detection and classification of subpixel spectral signatures in hyperspectral image sequences. University of Maryland, Baltimore County.

Helvacı, C. 1983. Bitlis Masifi Avnik (Bingöl) bölgesi metamorfik kayalarının petro-jenezi. Turk. J. Earth Sci, 26, 117-132.

Hempton, M. R. 1981. The East Anatolian transform fault: along strike variations in geometry and behavior. EOS Trans., 62, 393.

Hempton, M. R. 1987. Constraints on Arabian plate motion and extensional history of the Red Sea. Tectonics, 6 (6), 687-705.

Herece, E. 2008. Doğu Anadolu Fayı (DAF) Atlası. Özel Yayın Serisi.-13. Maden Tetkik ve Arama Genel Müdürlüğü. Jeoloji Etütleri Dairesi, Ankara.

Hewson, R. D., Cudahy, T. J., Huntington, J. F. 2001. Geologic and alteration mapping at Mt Fitton, South Australia, using ASTER satellite-borne data. In IGARSS 2001. Scanning the Present and Resolving the Future. Proceedings. IEEE 2001 International Geoscience and Remote Sensing Symposium, Cat. No. 01CH37217, Vol. 2, 724-726, IEEE.

Hewson, R. D., Cudahy, T. J., Mizuhiko, S., Ueda, K., Mauger, A. J. 2005. Seamless geological map generation using ASTER in the Broken Hill-Curnamona province of Australia. Remote Sensing of Environment, 99 (1-2), 159-172.

Holben, B., Justice, C. 1981. An examination of spectral band rationing to reduce the topographic effect on remotely sensed data. International journal of remote sensing, 2 (2), 115-133.

Hunt, G. R. 1977. Spectral signatures of particulate minerals in the visible and near infrared. Geophysics, 42 (3), 501-513.

Hunt, G. R., Salisbury, J. W. 1974. Mid-infrared spectral behavior of igneous rocks (Vol. 74, No. 625). Air Force Cambridge Research Laboratories, Air Force Systems Command, United States Air Force.

Hunt, G. R., Ashley, R. P. 1979. Spectra of altered rocks in the visible and near infrared. Economic Geology, 74 (7), 1613-1629.

Kayadibi, Ö. 2008. Mineral Haritalamada Bant Oranlama ve Crosta Metotları ile Elde Edilen Sonuçların Jeoistatiksel Olarak Karşılaştırılması. 2. Uzaktan Algılama ve Coğrafi Bilgi Sistemleri Sempozyumu, 13-15 Ekim, Kayseri.

Kriegler, F. J. 1969. Preprocessing transformations and their effects on multspectral recognition. In Proceedings of the Sixth International Symposium on Remote Sesning of Environment, 97-131.

Li, Q., Zhang, B., Lu, L., Lin, Q. 2014. Hydrothermal alteration mapping using ASTER data in Baogutu porphyry deposit, China. In IOP conference series: earth and environmental science, Vol. 17, No. 1, 012174, IOP Publishing.

Loughlin, W. P. 1991. Principal component analysis for alteration mapping. Photogrammetric Engineering and Remote Sensing, 57 (9), 1163-1169.

Lyberis, N., Yurur, T., Chorowicz, J., Kasapoğlu, E., Gündoğdu, N. 1992. The East Anatolian Fault: An oblique collisional belt. Tectonophysics, 204 (1-2), 1-15.

Mars, J. C., Rowan, L. C. 2011. ASTER spectral analysis and lithologic mapping of the Khanneshin carbonatite volcano, Afghanistan. Geosphere, 7 (1), 276-289.

McClusky, S., Balassanian, S., Barka, A., Demir, C., Ergintav, S., Georgiev, I., Gurkan, O., Hamburger, M., Hurst, K., Kahle, H., Kastens, K. 2000. Global Positioning System constraints on plate kinematics and dynamics in the eastern Mediterranean and Caucasus. Journal of Geophysical Research: Solid Earth, 105 (B3), 5695-5719.

McKenzie, D. 1972. Active tectonics of the Mediterranean region. Geophysical Journal International, 30 (2), 109-185.

Metin, S. 1972. Elazığ K44-a3 ve a4 paftalarının jeolojisi. Maden Tetkik ve Arama. Rapor no:16.

Ninomiya, Y. 2004. Lithologic mapping with multispectral ASTER TIR and SWIR data. In Sensors, Systems, and Next-Generation Satellites VII. Vol. 5234, 180-190, SPIE.

Ord, J. K., Getis, A. 1995. Local spatial autocorrelation statistics: Distributional issues and an application. Geographical analysis, 27 (4), 286-306.

Over, S., Kavak, K. Ş., Bellier, O., Özden, S. 2004. Is the Amik Basin (SE Turkey) a triple-junction area? Analyses of SPOT XS imagery and seismicity.

International Journal of Remote Sensing, 25 (19), 3857-3872.

Örgülü, G., Aktar, M., Türkelli, N., Sandvol, E., Barazangi, M. 2003. Contribution to the seismotectonics of Eastern Turkey from moderate and small size events. Geophysical Research Letters, 30 (24).

Özkaya, İ. 1978. Ergani-Maden yöresi stratigrafisi. Bulletin of the Geological Society of Turkey, August 21, 129-39.

Perinçek, D. 1979. Interrelations of the Arabian and Anatolian plates. InGuide Book Excursion B, First Geological Congress of the Middle East. Geological Society of Turkey, Ankara.

Perinçek, D., Çemen, I. 1990. The structural relationship between the East Anatolian and Dead Sea fault zones in southeastern Turkey. Tectonophysics, 172 (3-4), 331-340.

Pour, A. B., Hashim, M., Park, Y. 2017. Alteration mineral mapping in inaccessible regions using target detection algorithms to ASTER data. In Journal of Physics: Conference Series. Vol. 852, No. 1, 012022, IOP Publishing.

Pour, A. B., Park, Y., Park, T. Y. S., Hong, J. K., Hashim, M., Woo, J., Ayoobi, I. 2019. Evaluation of ICA and CEM algorithms with Landsat-8/ASTER data for geological mapping in inaccessible regions. Geocarto International, 34 (7), 785-816.

Reilinger, R. E., McClusky, S. C., Oral, M. B., King, R. W., Toksoz, M. N., Barka, A. A., Kinik, I., Lenk, O., Sanli, I. 1997. Global Positioning System measurements of present-day crustal movements in the Arabia-Africa-Eurasia plate collision zone. Journal of Geophysical Research: Solid Earth, 102 (B5), 9983-9999.

Rockwell, B.W. 2013. Automated mapping of mineral groups and green vegetation from Landsat Thematic Mapper imagery with an example from the San Juan Mountains, Colorado (No. 3252). US Geological Survey.

Rouskov, K., Popov, K., Stoykov, S., Yamaguchi, Y. 2005. Some applications of the remote sensing in geology by using of ASTER images. In Scientific Conf."SPACE, ECOLOGY, SAFETY" with Int. Participation, 167-173.

Rowan, L. C., Mars, J. C. 2003. Lithologic mapping in the Mountain Pass, California area using advanced spaceborne thermal emission and reflection radiometer (ASTER) data. Remote sensing of Environment, 84(3), pp.350-366.

Rowan, L. C., Schmidt, R. G., Mars, J. C. 2006. Distribution of hydrothermally altered rocks in the Reko Diq, Pakistan mineralized area based on spectral analysis of ASTER data. Remote sensing of Environment, 104 (1), 74-87.

Sabins, F. F. 1999. Remote sensing for mineral exploration. Ore geology reviews, 14 (3-4), 157-183.

Sirel, E., Metin, S., Sözeri, B. 1975. Palu (KD Elazığ) denizel Oligosen'in stratigrafisi ve mikropaleontolojisi. Türkiye Jeoloji Kurultayı Bülteni. 18 (2), 175-180.

Soytürk, N., Baştuğ, C. 1973. Kozluk-Baykan yöresi jeoloji raporu: TPAO; Rap. no. 795 (Unpublished).

Sümengen, M. 2011. 1:100 000 ölçekli Türkiye Jeoloji Haritası, Elazığ K-44 Paftası, 1-14. Jeoloji Etütleri Dairesi, Ankara.

Şaroğlu, F., Emre, Ö., Boray, A. 1987. Türkiye'nin Diri Fayları ve Depremsellikleri, Mineral Research and Exploration Institute Turkey, Report No. 8174 (in Turkish).

Şaroğlu, F., Emre, Ö., Kuşçu, İ. 1992*a*. Türkiye Diri Fay Haritası. MTA Genel Müdürlüğü, Ankara.

Şaroğlu, F., Emre, Ö., Kuşçu, İ. 1992*b*. The East Anatolian Fault zone of Turkey. Ann Tecton, 6, 99–125.

Şengör, A. M. C., Görür, N., Şaroğlu, F. 1985. Strike-slip faulting and related basin formation in zones of tectonic escape: Turkey as a case study.

Tangestani, M. H., Moore, F. 2002. Porphyry copper alteration mapping at the Meiduk area, Iran. International Journal of Remote Sensing, 23 (22), 4815-4825.

Taymaz, T., Eyidoğan, H., Jackson, J. 1991. Source parameters of large earthquakes in the East Anatolian Fault Zone (Turkey). Geophysical Journal International, 106 (3), 537-550.

Tözün, K. A. 2021. Kayseri çevresindeki olası metalik cevherleşmelerin uzaktan algılama ve jeokimyasal yöntemler kullanılarak incelenmesi. PhD Thesis. Kocaeli University, Institute of Science and Technology, 2021 (In Turkish).

USGS, 2004. https://earthexplorer.usgs.gov/.

USGS, 2004. http://speclab.cr.usgs.gov/spectral.lib04/spectral_lib.html.

Van der Meer, F. D., Van der Werff, H. M. A., Van Ruitenbeek, F. J. A. 2014. Potential of ESA's Sentinel-2 for geological applications. Remote sensing of environment, 1, 124-133.

Volesky, J. C., Stern, R. J., Johnson, P. R. 2003. Geological control of massive sulfide mineralization in the Neoproterozoic Wadi Bidah shear zone, southwestern Saudi Arabia, inferences from orbital remote sensing and field studies. Precambrian Research, 123 (2-4), 235-247.

Wang, J., Zhang, J. 2011. Study on clay alteration information extraction in vegetation coverage based on MTMF. In 2011 International Conference on Remote Sensing, Environment and Transportation Engineering, 8526-8529, IEEE.

Yamaguchi, Y., Naito, C. 2003. Spectral indices for lithologic discrimination and mapping by using the ASTER SWIR bands. International Journal of Remote Sensing, 24 (22), 4311-4323.

Zhang, X., Pazner, M., Duke, N. 2007. Lithologic and mineral information extraction for gold exploration using ASTER data in the south Chocolate Mountains (California). ISPRS Journal of Photogrammetry and Remote Sensing, 62 (4), 271-282.